Computational Materials Science 170 (2019) 109140

Contents lists available at ScienceDirect

Computational Materials Science

journal homepage: www.elsevier.com/locate/commatsci

A crystal-plasticity model of extruded AM30 magnesium alloy

Rongxin Zhou, Anish Roy*, Vadim V. Silberschmidt

Wolfson School of Mechanical, Electrical and Manufacturing Engineering, Loughborough University, LE11 3TU, United Kingdom

ARTICLE INFO

Keywords:
AM30
Grain size
Texture
Crystal plasticity
Finite-element analysis

ABSTRACT

An enhanced crystal-plasticity finite-element model is developed to model the effects of texture, grain size and loading direction on asymmetrical tension-compression behaviour of AM30 magnesium alloy. A constitutive description of plastic deformation in the suggested scheme accounts for contributions from deformation slip and twinning. The calibrated model was employed to investigate the effects of texture and grain size on the yield stress and strain-hardening behaviour of AM30 magnesium alloy at room temperatures under various loading conditions. The study reveals that grain refinement and initial texture significantly influence the mechanical behaviour of AM30. Results show that the key factor controlling the tension-compression asymmetry is deformation twinning. Two techniques, which could be used to reduce this asymmetry, are grain refinement and weakening of the initial texture in extruded AM30.

1. Introduction

Magnesium and its alloys have attracted significant attention in recent years as materials suitable for components in the automotive and biomedical sectors. This thanks to their attractive properties such as low density, high specific strength and excellent biocompatibility. However, magnesium and its alloys show a strong mechanical anisotropy, significant yield asymmetry in tension and compression [1,2] as well as poor ductility and formability at room temperature, which substantially restricts their widespread structural applications.

The observed mechanical characteristics are due to its hexagonal closed packed (HCP) crystallographic structure with a limited number of available slip systems. The possible slip systems in the HCP crystal structure include the basal $\langle a\rangle$, prismatic $\langle a\rangle$, pyramidal $\langle a\rangle$, first-order and second-order pyramidal $\langle c+a\rangle$ slip modes. Besides, three main twinning deformation systems can be identified in magnesium and its alloys, namely, extension twins $\{10\bar{1}2\}\langle 10\bar{1}1\rangle$, construction twins $\{10\bar{1}1\}\langle 10\bar{1}2\rangle$ and $\{10\bar{1}1\}$-$\{10\bar{1}2\}$ double twins [3,4]. Minimizing the asymmetry in mechanical properties may aid widespread commercial application of magnesium alloys. Previous studies demonstrated that several methods such as grain refinement [5–7], texture weakening [8–10], addition of rare-earth elements [1,11] and heat treatment [12] can be adopted to reduce this mechanical anisotropy. Among the above-mentioned methods, grain refinement and texture modification are considered the most efficient approaches as per experimental investigations. However, there are no studies which characterise the independent influence of grain size and texture on yield asymmetry and which of the two factors being the dominant one. Numerical modelling techniques have the capability to elucidate the influence of individual parameters such as grain size and texture accurately. Such an approach can lead to a better understanding of the physics of deformation in Mg and its alloys, which, in turn, can contribute to improving the design of components made from those materials.

Crystal-plasticity-based numerical models, accounting for different deformation modes, were used extensively to study deformation in crystalline materials including magnesium alloys [13–20]. Here, the visco-plastic self-consistent (VPSC) approach and the crystal-plasticity finite-element models (CPFEMs) were commonly used and implemented for a wide range of applications [14,21]. The VPSC scheme is a top-down modelling approach [19,20], with each grain treated as an ellipsoidal inclusion embedded in a homogeneous effective medium, representing the averaged behaviour of all other grains. It has some advantages in modelling the behaviour and texture evolution of large grain aggregates thanks to its relatively easy implementation in numerical simulations. However, grain interaction cannot be directly captured. Furthermore, the effect of a material's microstructure such as the grain boundary, grain shape and stress heterogeneity in each grain cannot be well represented either [22]. As a result, phenomena such as twin transmission [14] cannot be modelled. In contrast, the CPFEM is a bottom-up modelling approach, in which model parameters are determined using experimental studies in single-crystals. Based on this, a polycrystalline ensemble can be modelled at the mesoscale. Several CPFEM models were developed recently to study the deformation mechanisms of magnesium and its alloys [19,20,23].

* Corresponding author.
E-mail address: a.roy3@lboro.ac.uk (A. Roy).

https://doi.org/10.1016/j.commatsci.2019.109140
Received 30 December 2018; Received in revised form 6 July 2019; Accepted 14 July 2019

Nomenclature

HCP	hexagonal closed packed
VPSC	visco-plastic self-consistent
CPFEM	crystal-plasticity finite-element models
TT	tension twins
CT	construction twins
PTS	predominant twin system
RVE	representative-volume-element
ED	extruded direction
TD	transverse direction
CED	compression along the extruded direction
TED	tension along the extruded direction
45ED	45° to the extrusion direction

The current study aims to investigate the effects of grain size and texture intensity on the tension and compression deformation mechanisms as well as the observed tension-compression asymmetry in extruded AM30 at room temperature (T = 293 K). By studying the yielding stress and the strain-hardening behaviours of the magnesium alloy we try to understand the effects of texture and grain size on the mechanical behaviour of the extruded AM30.

The paper is organised as follows: A constitutive description of the crystal-plasticity model, accounting for the grain size effect in slip and twinning deformation modes, is introduced in Section 2. Section 3 presents the details of the computational framework including the finite-element model and calibration of the model parameters. Numerical simulations of the studied alloy are conducted in Section 4 for various grain sizes and texture intensities in uniaxial compression/tension along the extruded direction with the focus on discussing the deformation mechanisms accounting for the grain-size and texture effects. We conclude our study in Section 5.

2. Constitutive description

2.1. Kinematic slip and twinning

In CPFEM, the total deformation gradient $\boldsymbol{F}$ can be decomposed into elastic $\boldsymbol{F_e}$ and plastic $\boldsymbol{F_p}$ parts as

$$\boldsymbol{L}=\boldsymbol{F_e}\boldsymbol{F_p}. \tag{1}$$

The velocity gradient can be also identified as the elastic part and plastic part as

$$\boldsymbol{L}=\boldsymbol{L_e}+\boldsymbol{L_p}=\dot{\boldsymbol{F}}_{\boldsymbol{e}}\boldsymbol{F}_{\boldsymbol{e}}^{-1}+\boldsymbol{F_e}(\dot{\boldsymbol{F}}_{\boldsymbol{p}}\boldsymbol{F}_{\boldsymbol{p}}^{-1})\boldsymbol{F}_{\boldsymbol{e}}^{-1}. \tag{2}$$

Since Mg and its alloys possess an HCP crystallographic structure with a large aspect ratio, the plastic deformation can be derived from both crystalline slip and twinning. Therefore, in this study, the plastic part of the velocity gradient L_p includes the contributions from slip and twin deformations as

$$L_p = L_p^{sl} + L_p^{tw} + L_p^{sl-tw}, \tag{3}$$

where L_p^{sl}, L_p^{tw} and L_p^{sl-tw} respectively represent the plastic velocity gradient induced by the slip in the parent phase (untwined region), deformation twinning in the parent phase and secondary slip in the child phase (twined region). For clarity, the superscript α is used to represent the slip system in the parent phase, while β denotes for the twin system in the parent phase and $\tilde{\alpha}$ for the secondary slip system in the child phase. The three terms in Eq. (3) can be further expressed as

$$\begin{aligned}
\mathbf{L_p^{sl}} &= \left(1-\sum_{\beta}^{N_{tw}} f^{\beta}\right)\sum_{\alpha=1}^{N}\dot{\gamma}^{(\alpha)}\mathbf{s}^{(\alpha)}\otimes\ \mathbf{m}^{(\alpha)},\\
\mathbf{L_p^{tw}} &= \sum_{\alpha=1}^{N}\dot{\gamma}^{(\beta)}\mathbf{s}^{(\beta)}\otimes\ \mathbf{m}^{(\beta)},\\
\mathbf{L_p^{sl-tw}} &= \sum_{\beta}^{N_{tw}} f^{\beta}\sum_{\tilde{\alpha}=1}^{N_s}\dot{\gamma}^{(\tilde{\alpha})}\mathbf{s}^{(\tilde{\alpha})}\otimes\ \mathbf{m}^{(\tilde{\alpha})},
\end{aligned} \tag{4}$$

where $\dot{\gamma}^{(\alpha)}$ is the shear slip rate on the slip system α, f^{β} is the volume fraction of the child phase β and $\dot{\gamma}^{(\beta)}$ is the shear strain rate arising from deformation twinning. N_s and N_{tw} are the total number of slip and twin systems, respectively. The unit vectors $\mathbf{s}$ and $\boldsymbol{m}$ represent the direction in the slip/twin plane and the normal to it, respectively. Furthermore, the velocity gradient can be expressed in terms of a symmetric rate of stretching $\mathbf{D}$ and an antisymmetric rate of spin $\mathbf{W}$, i.e.

$$L = D + W = (D_e + W_e) + (D_p + W_p). \tag{5}$$

Using Eq. (2) and Eq. (5), it can be deduced

$$D_e + W_e = \dot{F}_e F_e^{-1},\ D_p + W_p = L_p^{sl} + L_p^{tw} + L_p^{sl-tw}. \tag{6}$$

2.2. Constitutive law

To account for the contributions from both parent and child twin phases, the Cauchy stress is averaged by the stress in these phases at each material point as

$$\overline{\boldsymbol{\sigma}} = \left(1-\sum_{\beta}^{N_{tw}} f^{\beta}\right)\boldsymbol{\sigma}_m + \sum_{\beta}^{N_{tw}} f^{\beta}\boldsymbol{\sigma}_{tw(\beta)}, \tag{7}$$

where $\boldsymbol{\sigma}_m$ and $\boldsymbol{\sigma}_{tw(\beta)}$ are the Cauchy stresses in the parent and child phases, respectively. In each phase, the constitutive law is expressed as the relationship between the elastic part of the stretching rate, $\mathbf{D_e}$, and the Jaumann rate of Cauchy stress, $\overset{\nabla}{\sigma}$, i.e.

$$\overset{\nabla}{\sigma}+\sigma(\mathbf{I}:\mathbf{D_e}) = \mathbf{C}:(\mathbf{D}-\mathbf{D_p}), \tag{8}$$

where $\mathbf{I}$ is the second-order unit tensor, $\mathbf{C}$ is the fourth-order, possibly anisotropic, elastic stiffness tensor. The Jaumann stress rate is expressed as

$$\overset{\nabla}{\sigma}=\dot{\sigma}-\mathbf{W_e}\sigma+\sigma\mathbf{W_e}. \tag{9}$$

On each slip system, the resolved shear stress, τ^{α}, is expressed by the Schmid law

$$\tau^{(\alpha)} = \mathbf{sym}(\mathbf{s}^{(\alpha)}\otimes\ \mathbf{m}^{(\alpha)}):\sigma. \tag{10}$$

The relationship between the shear rate $\dot{\gamma}^{(\alpha)}$ and the resolved shear stress $\tau^{(\alpha)}$ on the slip system α is expressed by the power law proposed by Hutchinson [24]

$$\dot{\gamma}^{(\alpha)} = \dot{\gamma}_0\left|\frac{\tau^{(\alpha)}}{g^{(\alpha)}}\right|^n \mathrm{sgn}(\tau^{(\alpha)}), \tag{11}$$

where $\dot{\gamma}_0$ is the reference shear rate, $g^{(\alpha)}$ is the slip resistance and n is the rate-sensitivity parameter.

Twinning is assumed to be essentially pseudo slip in the present study, thus the Schmid law is also adopted for twin systems. The shear strain rate of the twin deformation mode is assumed to be related with the evolution rate of the twinning volume fraction according to the equation

$$\dot{\gamma}^{\beta} = \gamma^{tw}\dot{f}^{\beta}, \tag{12}$$

where γ^{tw} is a constant, related with the aspect ratio of the crystal lattice. Therefore, the evolution rate of twinning volume fraction plays a crucial role in accounting for the twinning-induced deformation response. Experimental characterization of the rates of twin evolution in HCP materials is rare. A power-law relation was employed to describe the evolution of the twin volume fraction in previous studies [19,20].

However, this evolution seems to be exaggerated once twin deformation was activated. Experimental evidence [25–27] and numerical simulations [23] both demonstrated that twinning evolution generally stayed constant and might depend on the imposed strain rate. In this study, a combination of a power law and a constant rate was assumed to describe the evolution of the twinning volume fraction, as

$$\dot{f}^{\beta} = \begin{cases} \dot{f}_0 \left| \frac{\langle \tau^{\beta} \rangle}{\tau_c^{\beta}} \right|^m & \text{if } \tau^{\beta} < \tau_c^{\beta} \\ k\dot{f}_0 & \text{if } \tau^{\beta} \geqslant \tau_c^{\beta} \end{cases},$$

$$\langle \tau^{\beta} \rangle = \begin{cases} \tau^{\beta} & \text{if } \tau^{\beta} > 0 \,\&\, f_{\Sigma}\left(= \sum_{\beta}^{N_{tw}} f^{\beta}\right) \leqslant f_{cr} \\ 0 & \text{otherwise} \end{cases}, \tag{13}$$

where $\dot{f}_0$ is the reference rate of the twin volume fraction, which is dependent on the imposed strain rate in the sample, k is an empirical value, which only dependent on the imposed strain rate, τ^{β} is the corresponding resolved shear stress, τ_c^{β} is the resistance to deformation twinning, m is the rate-sensitivity parameter and f_{cr} is the critical twin volume fraction, which represents the saturation value of the twin in a material point. Once the critical volume fraction is reached, the lattice in the corresponding material point invokes reorientation [19,20].

2.3. Hardening law accounting for the grain-size effect

The hardening law, which captures the evolution of slip resistance, is defined as

$$g^{\alpha} = g_0^{\alpha} + g_f^{\alpha} + g_{HP}^{\alpha}. \tag{14}$$

Similarly, the resistance to deformation twinning may be expressed as

$$g^{\beta} = g_0^{\beta} + g_f^{\beta} + g_{HP}^{\beta}, \tag{15}$$

where g_0, g_f and g_{HP} are the initial lattice resistance, forest-dislocation interaction and resistance of the barrier imposed by grain/twin boundaries, respectively.

2.3.1. Forest-dislocation interaction

Due to twinning modes, forest-dislocation interaction in a slip system, g_f^a, should account for both slip-slip and twinning-slip interactions. Thus, this is expressed as

$$g_f^a = g_{f,sl\leftrightarrow sl}^{\alpha} + g_{f,tw\rightarrow sl}^{\alpha} = \sum_{\alpha'=1}^{N_s} g_{f,\alpha'}^{\alpha} + \sum_{\beta=1}^{N_{tw}} g_{f,\beta}^{\alpha}, \tag{16}$$

where $g_{f,sl\leftrightarrow sl}^{\alpha}$ and $g_{f,tw\rightarrow sl}^{\alpha}$ are the slip resistance due to slip-slip and twin-slip interactions, respectively. For the slip-slip interaction, $g_{f,sl\leftrightarrow sl}^{\alpha}$, both the self- slip-slip interaction (i.e. when $\alpha = \alpha'$) and latent slip-slip interaction (i.e. when $\alpha \neq \alpha'$) are incorporated into the system. And the relation between these two interactions are obtained as

$$g_{f,\alpha'}^{\alpha} = q_{\alpha\alpha'} g_{f,\alpha'}^{\alpha'}, \tag{17}$$

where $q_{\alpha\alpha'}$ is the latent interaction coefficient that typically ranges between 1 and 2. In this study, it is assumed that $q_{\alpha\alpha'} = 1$. Here, $g_{f,\alpha'}^{\alpha'}$ is the self-resistance in each slip system, which can be further identified as the self-resistance of basal slip, $g_{f,basal}^{\alpha'}$, and the self-resistance of non-basal slip $g_{f,non-basal}^{\alpha'}$due to different interaction mechanisms. The hardening rate of self-resistance then can be expressed according to [28], as:

$$\dot{g}_f^{\alpha'} = \begin{cases} h_0^{basal} \dot{\gamma}^{\alpha'} & \text{(basal slip)} \\ h_0^{\alpha'} \operatorname{sech}^2\left(\frac{h_0^{\alpha'}\gamma}{g_s^{\alpha'} - g_0^{\alpha'}}\right)\dot{\gamma}^{\alpha'} & \text{(non - basal slip)} \end{cases}, \quad \gamma = \sum_{\alpha'=1}^{N_s} \int_0^t |\dot{\gamma}^{\alpha'}| \, dt, \tag{18}$$

where $h_0^{\alpha'}$ refers to the initial hardening modules and $g_s^{\alpha'}$ is the saturation stress in each slip system.

The resistance induced by the twin-slip systems $\tau_{f,tw\rightarrow sl}^{\alpha}$ should account for the effects of extension twins (TT) and construction twins (CT) on the slip systems separately as:

$$g_{f,tw\rightarrow sl}^{\alpha} = g_{f,TT\rightarrow sl}^{\alpha} + g_{f,CT\rightarrow sl}^{\alpha} = \sum_{\beta=1}^{N_{TT}} g_{f,\beta}^{\alpha} + \sum_{\beta=1}^{N_{CT}} g_{f,\beta}^{\alpha}, \tag{19}$$

where N_{TT} and N_{CT} are the number of twin deformation systems in TT and CT respectively. Similar to the latent interaction between different slip systems, the TT-slip resistance is formulated as

$$g_{f,\beta}^{\alpha} = q_{TT\rightarrow\alpha} g_{f,TT}^{\beta} (\text{TT} \rightarrow \text{slip}). \tag{20}$$

Here, $g_{f,TT}^{\beta}$ is the self-resistance to TT of the system β, and $q_{TT\rightarrow\alpha}$ is the interaction factor between TT and slip systems. Similar to the slip-based interactions defined in Eq. (17), the hardening rate of self-resistance in TT can be expressed as

$$\dot{g}_{f,TT}^{\beta} = h_0^{\beta} \operatorname{sech}^2\left(\frac{h_0^{\beta}\gamma_{TT}}{g_s^{\beta} - g_0^{\beta}}\right)\dot{\gamma}^{\beta}, \quad \gamma_{TT} = \sum_{\beta=1}^{N_{TT}} \int_0^t |\dot{\gamma}^{\beta}| \, dt, \tag{21}$$

where h_0^{β} and g_s^{β} are the initial hardening modulus and the saturation stress in TT deformation mode, respectively.

The CT-induced resistance on the slip systems is considered to depend on the total volume fraction accumulated over all the activated construction twining systems, following the work in [19] as

$$g_{f,CT\rightarrow sl}^{\alpha} = \sum_{\beta=1}^{N_{CT}} g_{f,\beta}^{\alpha} = H_{CT\rightarrow sl}\left(\sum_{\beta=1}^{N_{CT}} f_{CT}^{\beta}/\gamma_{CT}^{tw}\right)^{0.5} \quad (\text{CT} \rightarrow \text{slip}), \tag{22}$$

where $H_{CT\rightarrow sl}$ denotes the initial hardening parameter of the CT-slip interaction.

For the twinning-based deformation, the contribution from twin-twin ($g_{f,tw\leftrightarrow tw}^{\beta}$) and slip-twin ($g_{f,sl\rightarrow tw}^{\beta}$) interactions may be considered for g_f^{β} as

$$g_f^{\beta} = g_{f,tw\leftrightarrow tw}^{\beta} + g_{f,sl\rightarrow tw}^{\beta} = \sum_{\beta'=1}^{N_{tw}} g_{f,\beta'}^{\beta} + \sum_{\alpha=1}^{N_s} g_{f,\alpha}^{\beta}. \tag{23}$$

However, experimental evidence [29,30] demonstrated that the effect of slip on both TT and CT are insignificant. Hence this resistance is neglected in our study.

The TT-TT and CT-CT interactions may be crucial due to different mechanisms underlying the evolution of TT and CT [19]. Thus, $g_{f,tw\leftrightarrow tw}^{\beta}$ can be expressed as

$$g_{f,tw\leftrightarrow tw}^{\beta} = g_{f,TT\leftrightarrow TT}^{\beta} + g_{f,CT\leftrightarrow CT}^{\beta} = \sum_{\beta'=1}^{N_{TT}} g_{f,\beta'}^{\beta} + \sum_{\beta'=1}^{N_{CT}} g_{f,\beta'}^{\beta}. \tag{24}$$

The resistance due to TT-TT interaction is expressed as

$$g_{f,\beta'}^{\beta} = q_{TT} g_{f,TT}^{\beta'} (\text{TT}), \tag{25}$$

where q_{TT} is the interaction coefficient between the TT systems and assumed to be 1 in our study.

Following the work in [19,20], the evolution law for the CT-CT interaction may be expressed as

$$\dot{g}_{f,CT\leftrightarrow CT}^{\beta} = \sum_{\beta'=1}^{N_{CT}} g_{f,\beta'}^{\beta} = H_{CT\leftrightarrow CT}\left(\sum_{\beta'=1}^{N_{CT}} f^{\beta'}\right)^{\eta} \dot{\gamma}^{\beta}, \tag{26}$$

where $H_{CT\leftrightarrow CT}$ and η are empirical parameters controlling the hardening rate of CT-CT interaction.

2.3.2. Resistance of grain and twin boundaries

To account for the effect of grain size on the mechanical behaviour of AM30, an expression similar to the classical Hall-Petch effect was incorporated into the hardening law by defining a third term as:

$$\tau_{HP}^{\alpha} = \mu^{\alpha} H_I^{\alpha} \sqrt{\frac{b^{\alpha}}{d^{\alpha}}}. \tag{27}$$

Here, μ^{α} and b^{α} are the shear modulus and Burgers vector of slip system α, respectively. H_I^{α} is the material parameter depending on the slip mode, with the subscript I indicating three possible conditions: $I = 0$ indicates no child phase in the grain; $I = 1$ implies a predominant child phase resulting from TT and $I = 2$ – a predominant child phase resulting from CT. Depending on the choice of I, the parameter d represents the grain size d_g when $I = 0$ or the mean free path between the adjacent child phases, d_{mfp}^{α}, when $I = 1$ or $I = 2$ as shown in Fig. 1. The presence of a child phase in a crystal (twin boundaries) introduces an additional barrier for dislocation motion, which manifests in the classical Hall-Petch effect. The mean free path, d_{mfp}^{α}, depends on the orientation between the predominant child phase and the slip plane, which is expressed as

$$d_{mfp}^{\alpha} = \frac{(1 - f^{PTS})\lambda d_g}{\sin\theta}, \tag{28}$$

where f^{PTS} is the volume fraction of the predominant twin system (PTS) in the crystal, $\lambda$is the ratio of the twin spacing and grain size, and θ is the angle between the plane of PTS and the slip plane.

For twinning deformation mode, the resistance of the barrier of grain or twin boundaries may be defined as:

$$\tau_{HP}^{\beta} = \begin{cases} \frac{H^{\beta}}{\sqrt{d_g}} & f_{\sum} = 0 \quad \text{or} \quad \beta = \text{PTS} \\ \frac{H^{\beta}}{\sqrt{d_{mfp}}} & f_{\sum} > 0 \quad \text{and} \quad \beta \neq \text{PTS} \end{cases}, \tag{29}$$

where H^{β} is the Hall-Petch coefficient.

It should be noted here that the CPFEM developed can account for the temperature and strain-rate effects on the mechanical behaviour of the magnesium alloy. To accomplish this, the initial CRSS, the resistance from grain or twin boundaries and the resistance from the deformation interaction, in the hardening law should be defined as a function of temperature and strain rate. In this study, the focus is on the effects of texture intensity and the grain size on the mechanical behaviour of the extruded AM30 and, thus, the development of temperature- and strain-rate-dependent functions in the hardening law is left for the future studies. Some details are available in [20].

Strain-gradient based approaches may be incorporated to capture the grain-size dependence in crystal plasticity instead of the Hall-Petch effect inspired relation in equation (27), however, these approaches have drawbacks including assigning physically relevant boundary conditions. A possible approach which may reduce some of the phenomenology is to implement field dislocation mechanics [31] which account for dislocation evolution and generation while accounting for grain-boundary effects in a physically reasonable way [32].

3. Computational framework

3.1. Finite element model

In this study, the CPFEM was implemented in Abaqus/Explicit by employing the user subroutine (VUMAT). The scheme of this subroutine was developed from a user subroutine (UMAT) introduced in the work of Huang [33]. The stress update algorithm used in ABAQUS/Explit environment is different from the one used in ABAQUS/Standard. The former employed the Green-Naghdi stress rate while the later was based on the Jaumann stress rate. Therefore, stress update algorithm incorporated was

$$\sigma|_{t+\Delta t} = \Delta\mathbf{R}\sigma|_t \Delta\mathbf{R}^{\mathbf{T}} + \mathbf{R}\Delta\sigma\mathbf{R}^{\mathbf{T}} \tag{30}$$

where $\Delta\mathbf{R}$ is the relative spin increment tensor, $\Delta\sigma$ is the stress increment obtained with the Jaumann stress rate and $\mathbf{R}$ is the rotation tensors decomposed from the total deformation gradient $\mathbf{F}$. Since the stress and strain tensors in ABAQUS/Explicit are defined based on the spatial coordinate system (i.e. with respect to the local coordinate system rotating with the volume) instead of the fixed global coordinate system, the finite strain theory is incorporated in the current study.

A modelling approach based on 3D representative-volume-element (RVE) was used to investigate the deformation mechanisms of the extruded AM30 alloy under various loading conditions. The RVE model has a side length of 200 μm, with 5 grains in each direction, as shown in Fig. 2. We carried out a mesh sensitivity analysis in tension and compression for a fully random texture (Fig. 3(a2)) as well as a strong initial basal texture with an intensity of 0.8 (Fig. 3(a1)). The results indicate that a mesh of $2 \times 2 \times 2$ elements for each grain was sufficient when compared to results obtained from a mesh of $4 \times 4 \times 4$ elements for each grain. Therefore, each grain was meshed with $2 \times 2 \times 2$ first-order hexahedral reduced-integration elements (C3D8R elements in ABAQUS) for the study. To validate the sufficiency of the number of grains in the chosen RVE ($5 \times 5 \times 5 = 125$ grains), a grain convergence study was performed. Two additional virtual microstructures containing $2 \times 2 \times 2 = 8$ grains and $8 \times 8 \times 8 = 512$ grains were employed as potential RVEs. Simulations with fully random texture and strong basal texture for both uniaxial compression and tension along the ED were conducted. A convergence plot with different grain numbers in compression is shown in Fig. 3(b1), (b2) for a strong basal texture and a random texture, respectively. The random orientations of the grains are generated by using random generation functions for Euler angles, which are incorporated into the python codes for pre-processing of the finite element model. The results suggest that $5 \times 5 \times 5$ grains are representative of the microstructure and used for all modelling work in this study. Uniaxial compression/tension was imposed by deforming the $+X$ face along the X axis with the $-X$ face constrained in displacing in the x-direction. Periodic boundary condition imposed on the Y and Z faces.

For simplification and without loss of generality, four slip planes -basal, prismatic, pyramidal $\langle a \rangle$ and pyramidal $\langle c + a \rangle$- and two twinning deformations -extension twin (TT) and contraction twin (CT)- are considered (Table 1) with the corresponding slip and twin planes shown in Fig. 4.

3.2. Model verification and parameters calibration

Mg and its alloys are characterised by a wide variety of possible deformation systems. Hence, a thorough understanding of the deformation mechanisms including characterisation of the critical resolved shear stress as well as the hardening rate during the deformation for each slip/twin system is essential. Here, experimental data obtained from uniaxial compression tests at various temperatures and strain rates

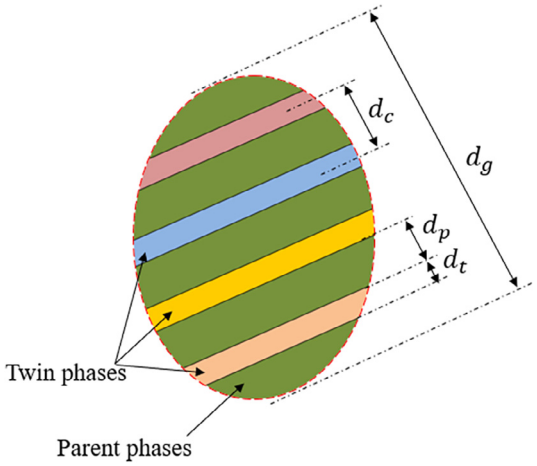

Fig. 1. Schematic of grain/twin boundaries.

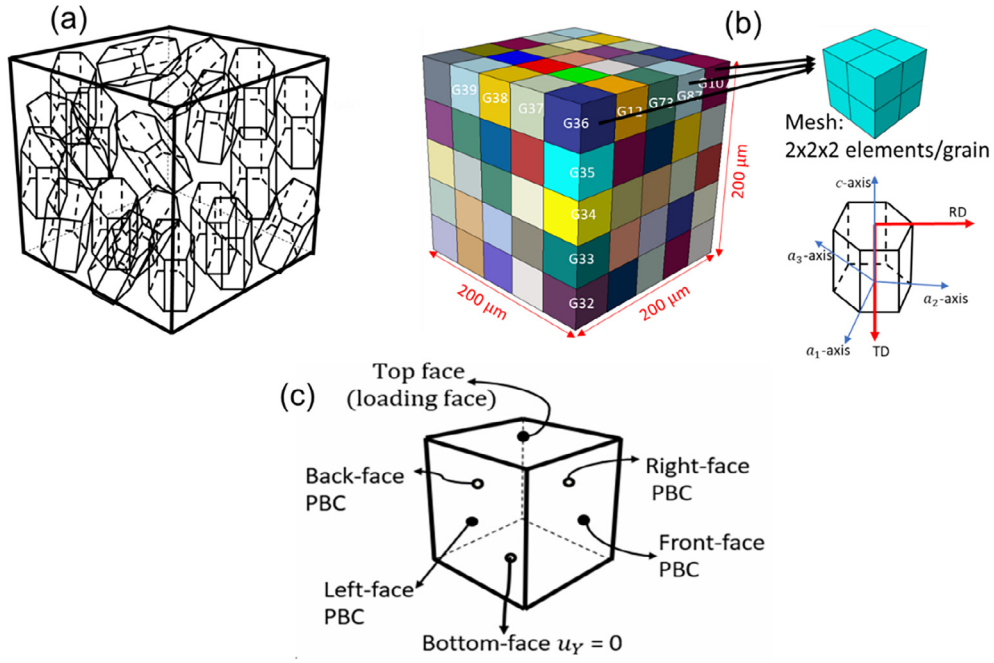

Fig. 2. 3D RVE model of extruded AM30: (a) crystal orientation in the RVE; (b) each cube in the RVE representing a grain; (c) loading and boundary conditions.

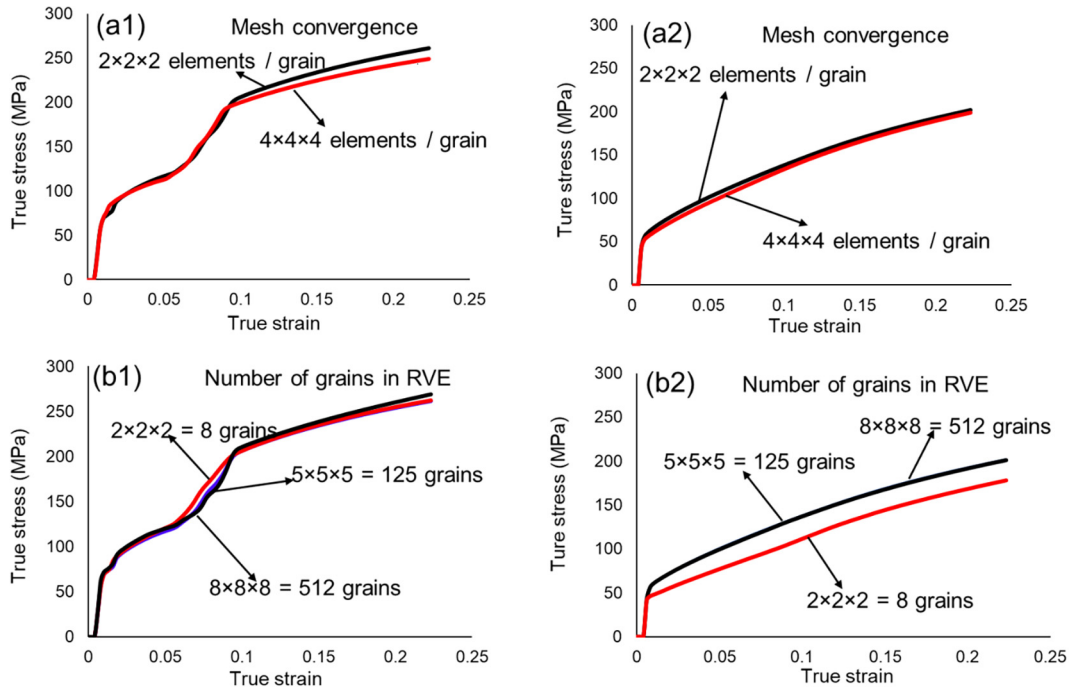

Fig. 3. Mesh convergence in compression: (a1) strong basal texture, (a2) random texture; and number of grains convergence studies: (b1) strong basal texture, (b2) random texture.

Table 1
Slip and twin systems considered for magnesium.

	Slip/twin plane	Slip/twinning direction	Number of modes
Basal	{0001}	$\langle 11\bar{2}0\rangle$	3
Prismatic	$\{10\bar{1}0\}$	$\langle 11\bar{2}0\rangle$	3
Pyramidal $\langle a\rangle$	$\{10\bar{1}1\}$	$\langle 11\bar{2}0\rangle$	6
Pyramidal $\langle c+a\rangle$	$\{11\bar{2}2\}$	$\langle 11\bar{2}3\rangle$	6
Extension twin (TT)	$\{10\bar{1}2\}$	$\langle 10\bar{1}1\rangle$	6
Contraction twin (CT)	$\{10\bar{1}1\}$	$\langle 10\bar{1}\bar{2}\rangle$	6

were used to calibrate the model. An initial texture was introduced based on microstructured observations. The extruded AM30 exhibits a strong basal texture in the TD-RD plane, with the basal intensity in the TD-RD being higher than 80% [34]. So, in the model, ~80% of grains were assigned a basal texture in the TD-RD plane, and remaining grains were randomly oriented. A reasonable correlation between the experimental stress-strain curves and the CPFEM predictions for all the loading cases was achieved after calibration (Fig. 5).

Key constitutive equations and model parameters related to the slip and twin deformation modes at the reference temperature T = 293 K and strain rate of $10^{-1}\,s^{-1}$ in the CPFEM model are summarised in

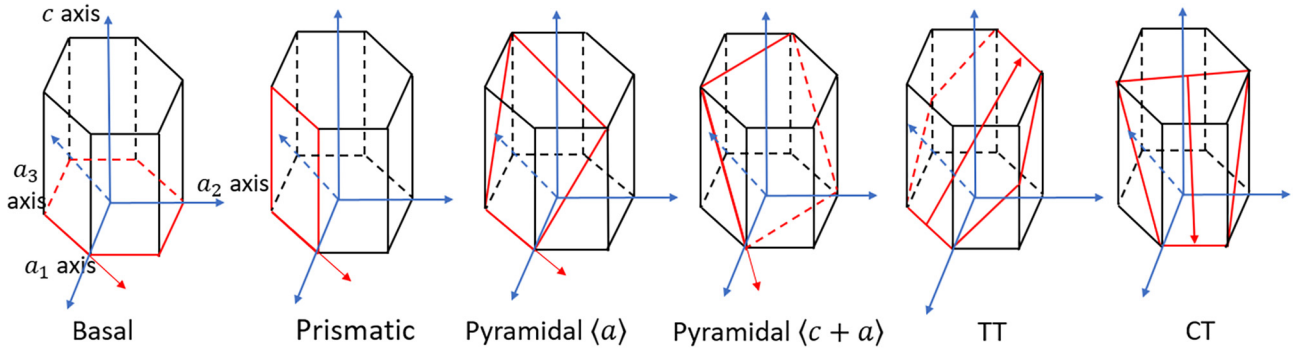

Fig. 4. Slips and twin systems in magnesium alloy.

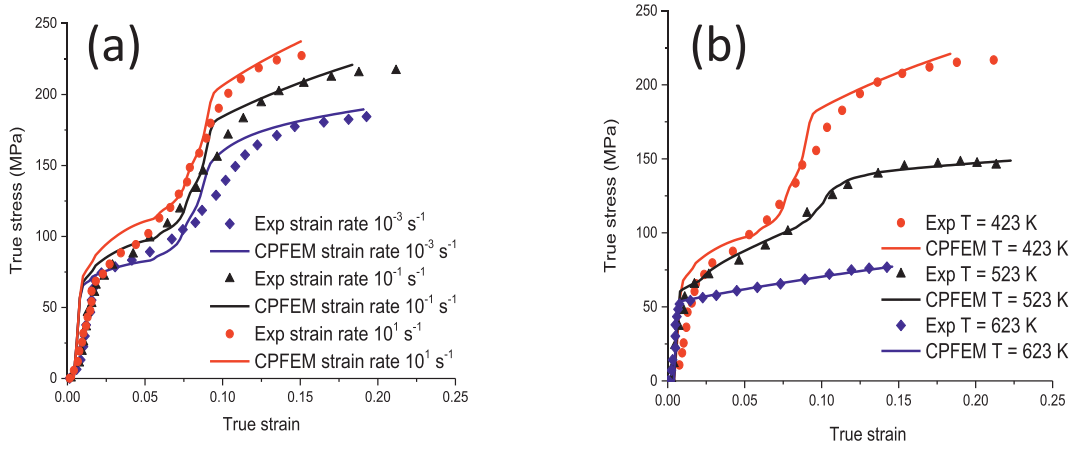

Fig. 5. Model verification with experimental results: (a) different strain rate; (b) different temperature.

Table 2.

The anisotropic elasticity of the alloy is characterized by 5 independent elastic constants C_{11}, C_{12}, C_{13}, C_{33} and C_{44}, with $C_{55} = C_{66} = (C_{11} - C_{12})/2$. The corresponding values for these elastic constants are listed in Table 3.

3.3. Relative activity of deformation modes

To assess the contributions of slip and deformation twinning to macroscopic plastic deformation, the relative activity of each slip and twin system was calculated in the simulation during the entire loading history.

Table 2
Key slip and twin constitutive equations and related parameters (length in μm, stress in MPa) ('–' denotes unavailable parameters) at reference conditions: T = 293 K and strain rate $10^{-1}\,s^{-1}$.

Shear-strain evolution law								
$\dot{\gamma}^{(\alpha)} = \dot{\gamma}_0 \left\lvert \frac{\tau^{(\alpha)}}{g^{(\alpha)}} \right\rvert^n \mathrm{sgn}(\tau^{(\alpha)})$		(11)						$\dot{\gamma}_0 = 0.1,\ n = 20$
$\dot{f}^{\beta} = \dot{f}_0 \left\lvert \frac{\langle \tau^{\beta} \rangle}{\tau_c^{\beta}} \right\rvert^m$ or $k\dot{f}_0$		(13)						$\dot{f}_0 = 0.1,\ m = 20,\ k = 1$
Hardening law								
$g = g_0 + g_f + g_{HP}$	(14) and (15)			Basal	Prism	Pyr < a >	Pyr < c + a >	TT	CT
g_0:			g_0	12	75	75	160	15	200
g_f:	$\dot{g}_f = h_0 \mathrm{sech}^2\left(\frac{h_0 \gamma}{s_s - s_0}\right)\dot{\gamma}$ or $h_0^{basal}\dot{\gamma}^{\alpha'}$	(18) and (21)	h_0	50	1500	1500	3000	100	–
			s_s	–	400	400	800	20	–
	$g^{\alpha}_{f,CT\to sl} = H_{CT\to sl}\left(\sum_{\beta=1}^{N_{CT}} f^{\beta}_{CT}/\gamma^{tw}_{CT}\right)^{0.5}$	(22)	$H_{CT\to sl}$	50	50	50	50	–	–
	$\dot{g}^{\beta}_{f,CT\leftrightarrow CT} = H_{CT\leftrightarrow CT}\left(\sum_{\beta'=1}^{N_{CT}} f^{\beta'}\right)^{\eta}\dot{\gamma}^{\beta}$	(26)	$H_{CT\leftrightarrow CT}$	–	–	–	–	–	9000
			η	–	–	–	–	–	0.5
g_{HP}:	$\tau^{\alpha}_{HP} = \mu^{\alpha} H_I^{\alpha}\sqrt{\frac{b^{\alpha}}{d^{\alpha}}}$	(27)	H_0^{α}	0.1	0.25	0.25	0.4	–	–
			H_1^{α}	0.4	0.6	0.6	0.8	–	–
			H_2^{α}	0.5	0.8	0.8	1.2	–	–
			b^{α}	3.21e-4	3.21e-4	6.12e-4	1.09e-4	–	–
	$\tau^{\beta}_{HP} = H^{\beta}/\sqrt{d_g}$ or $H^{\beta}/\sqrt{d_{mfp}}$	(29)	H^{β}	–	–	–	–	40	100

Table 3
Elastic constants of AM30 (in GPa) at reference conditions: T = 293 K and strain rate $10^{-1}\,s^{-1}$.

C_{11}	C_{12}	C_{13}	C_{33}	C_{44}	C_{55}
63.4	25.9	21.7	66.4	18.4	18.8

Following the work in [20], the relative activity in an activated phase is defined as

$$r^{\alpha} = \frac{\sum_{\alpha' \in \alpha} \dot{\gamma}^{\alpha'}}{\sum_{\alpha'=1}^{N_{sl}} \dot{\gamma}^{\alpha'} + \sum_{\beta'=1}^{N_{tw}} \dot{\gamma}^{\beta'}} \ (\text{slip mode}), \tag{31}$$

$$r^{\beta} = \frac{\sum_{\beta' \in \beta} \dot{\gamma}^{\beta'}}{\sum_{\alpha'=1}^{N_{sl}} \dot{\gamma}^{\alpha'} + \sum_{\beta'=1}^{N_{tw}} \dot{\gamma}^{\beta'}} \ (\textit{twin mode}), \tag{32}$$

for the slip r^{α} and twin r^{β} modes, respectively. To obtain the relative activity of a slip or twin mode in the studied sample of extruded AM30, the volume fraction averages of r^{α} and r^{β} were calculated for all the grains in the RVE.

4. Results and discussion

In this section, the grain size and texture intensity of the extruded AM30 are studied with emphasis on critical assessment of the underlying deformation mechanisms.

4.1. Tension-compression asymmetry in extruded AM30

Loading HCP crystalline materials along its *c*-axis, typically favour two mechanisms which accommodate plastic strain. These are the extension twins and the second pyramidal $< c + a >$ slip, with the crystal structure elongating along the *c*-axis. Therefore, on applying a compressive load along the extruded direction, which tends to extend the crystal lattice along the *c*-axis, plastic strain usually begins with extension twinning. The basal slip was not activated initially since its Schmid factor was negligibly small. An example of the loading condition elongating the HCP crystal along its *c*-axis is uniaxial compression along the extruded direction (CED). On the other hand, a stress state leading to a contraction of the HCP crystal lattice along the *c*-axis is accompanied by dislocation slip as extension twins cannot be activated in this loading case. Limited contraction twinning can be identified under this loading condition, as contraction twins are largely inactive when compared to extension twins due to the former's high CRSS [19]. An example of a stress state resulting in contraction along the *c*-axis is uniaxial tension along the extruded direction (TED).

Mechanical responses of the extruded AM30 under TED and CED for the same conditions, i.e. temperature T = 293 K and strain rate 0.1 s^{-1}, is shown in Fig. 6. As expected, the extruded AM30 demonstrated a remarkable tension-compression deformation asymmetry, with the true stress-strain curve in compression (CED) showing a dominant extension twinning activity, which yielded a double-hardening response. Also, the yield stress in the compression sample (CED) was less than that in the tension sample (TED) for the same imposed strain, this is attributed to an ease activation of extension twin in this sample. The tension-compression deformation asymmetry along ED for magnesium alloy was experimentally observed in [25]. The numerical results reproduce the experimental observations reasonably well.

Analysis of the relative activity of deformation modes shown in Fig. 6(b) further elucidates the tension-compression asymmetry observed. In the CED test, twinning initiated plasticity while all other mechanisms had a significantly lower contribution. In contrast, the TED test showed that non-basal slips, such as prismatic and pyramidal slips, dominated, and contributed substantially to, plastic deformation. High CRSSs in these non-basal slips contributes to the rise of the yield stress in TED. This confirms that the underlying activation of different deformation modes in TED and CED resulted in the asymmetrical

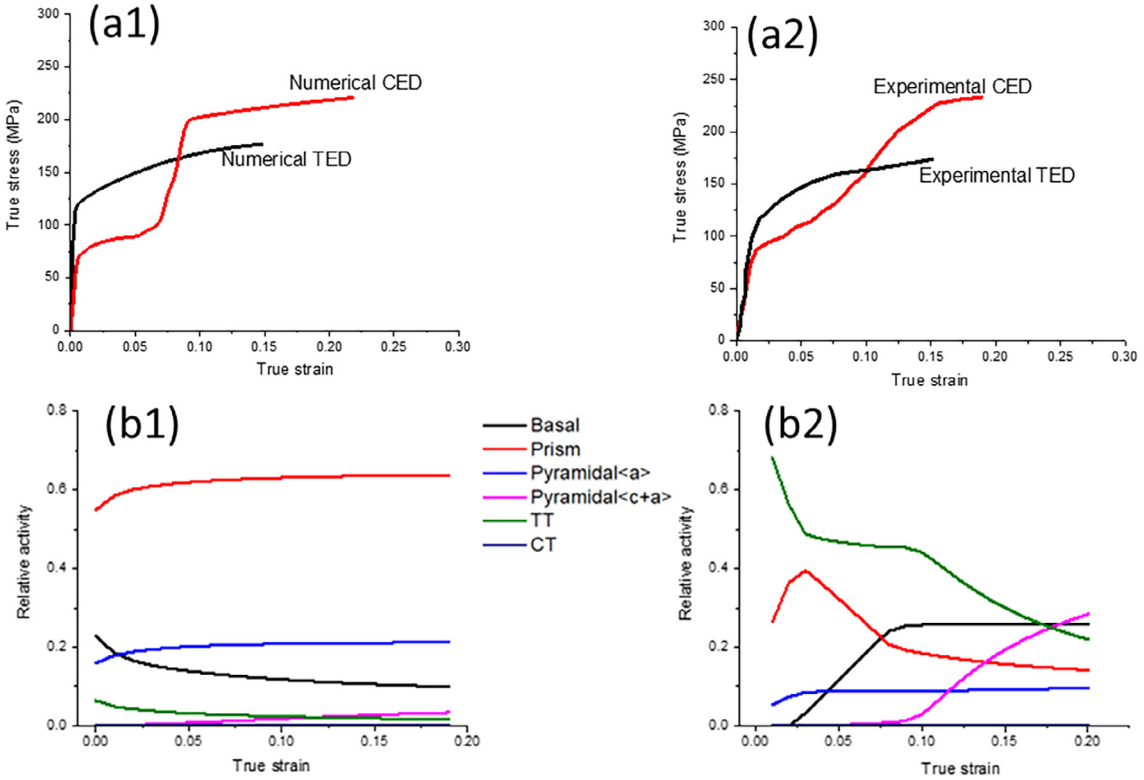

Fig. 6. Tension-compression asymmetry of extruded AM30: (a1) numerical true stress-strain curves; (a2) experimental true stress-strain curves [25]; (b1) relative activity in tension; (b2) relative activity in compression.

macroscopic behaviour of the extruded AM30.

4.2. Texture-intensity effects

An extrusion process induces a strong texture in the material with the basal plane parallel to the extruding direction. Thus, it is reasonable to expect that the basal texture intensity would play an important role in the tension-compression asymmetry in the extruded AM30. Here, various initial basal texture intensities attributed to the RVE model are studied. This texture intensity was defined as the ratio of the number of grains with a basal orientation to the total number of the grains in the RVE. Thus, in this study, a zero value of basal texture intensity refers to a totally random texture while a value of 1 implies a single crystal with basal texture in the RVE model. Studies of both uniaxial tension and compression were conducted at the same loading conditions of T = 293 K and an imposed strain-rate of $0.1\,s^{-1}$. For the loading in tension and compression with the same initial texture intensity, the same initial microstructures were used in the models. The pole figure of the initial microstructure is shown in Fig. 7.

The effect of texture intensity in the TED orientation is presented in terms of true stress-strain curves as shown in Fig. 8. The yield stress and the hardening behaviour were strongly influenced by the chosen initial texture intensity. In general, with an increase in basal texture intensity, the yield stress was observed to increase. To further illustrate the nuances of the deformation modes, an RVE model with a fully random texture, a single crystal and a basal texture intensity of 0.5 were studied (Fig. 8(b)). Apparently, for the single-crystal sample (i.e. basal texture intensity = 1) (Fig. 8(b3)), the non-basal prismatic slip dominated the plastic deformation followed by the pyramidal slip during all the deformation stage, with the basal slip contributing nearly nothing to plasticity. With a reduction in the basal texture intensity, viz. the case with random orientation (basal texture intensity = 0) (Fig. 8(b1)), the relative contribution of basal induced slip increased as there were grains with favourable orientations that sustained this deformation mode, resulting in a reduction of the yield stress.

Twinning activity was also observed in deformation in the TED tests, although its impact was much lower compared with other deformation modes. In relative terms, such activity reduced with an increase in the basal texture intensity (Figs. 6(b) and 8(b)). The effect of texture intensity on the twinning activity for TED in numerical experiments is shown in Fig. 9. The colours indicate different twinning phases that have been activated (e.g. blue colour indicates the number of phases equal to 1, which implies that only the parent phase was active; consequently, a red colour indicate the number of phases equal to 7, which implies six activated child phases). Clearly, the number of activated twins decreased with an increase in basal intensity. When it increased to 1 (i.e. a case of the single-crystal sample), no twinning was observed in the model under this loading condition, indicating that the Schmid factor for extension twinning was zero.

This effect of texture in CED was drastically different. There was no obvious trend in the yield stress (around 0.2% proof stress) with a change in the basal texture intensity. A sample with a random texture showed a lower yield stress (Fig. 10), whereas the sample with a basal texture intensity of 0.5 demonstrated the highest yield stress. Relative activity of the deformation modes in the sample with a totally random texture, a single crystal and the sample with a basal texture intensity of 0.5, is shown in Fig. 10(b). It is apparent that the activities of the deformation modes were significantly affected by the texture intensity of the sample. In the sample with a random texture, the basal slip system dominated the plastic deformation due to its relatively lower CRSS, which leads to a lower yield stress in this sample. With an increase in the basal texture intensity up to 0.5, the non-basal slip, such as prismatic and pyramidal slips, was activated, effectively increasing the overall yield stress. With a further increase in basal texture intensity (> 0.5), extension twins increasingly dominated the deformation process, leading to a double-hardening response and a decrease in the yield stress. As expected, the texture intensity strongly affected the deformation twinning activity (Fig. 11), with more twin phases activated with an increase in the basal texture intensity. For the sample with a strong basal texture intensity (≥ 0.8), deformation twins were found in almost all the grains of the RVE.

The tension-compression asymmetry reduced as the basal texture intensity weakened. It vanishes in a sample with a fully random texture (Figs. 8(a) and 10(a)). It is interesting to note that the deformation modes in TED and CED for a fully random texture were similar (Fig. 8(b) and 10(b)), with basal slip dominating the overall deformations with a low activity from deformation twinning. It can be concluded that magnesium alloys with a random texture will exhibit the yield symmetry while a strong basal texture results in a significant asymmetry in TED and CED deformation modes.

The pole figures indicating the texture after deformation at a strain of ~10% for different initial texture intensities are shown in Fig. 12. By comparing the initial texture (Fig. 7) with a high intensity (e.g. texture intensity = 0.8 or the single crystal), basal planes tend to reorient perpendicularly to the compression direction, thus, aligning the c-axis parallel to the loading direction. Consequently, subsequent plastic

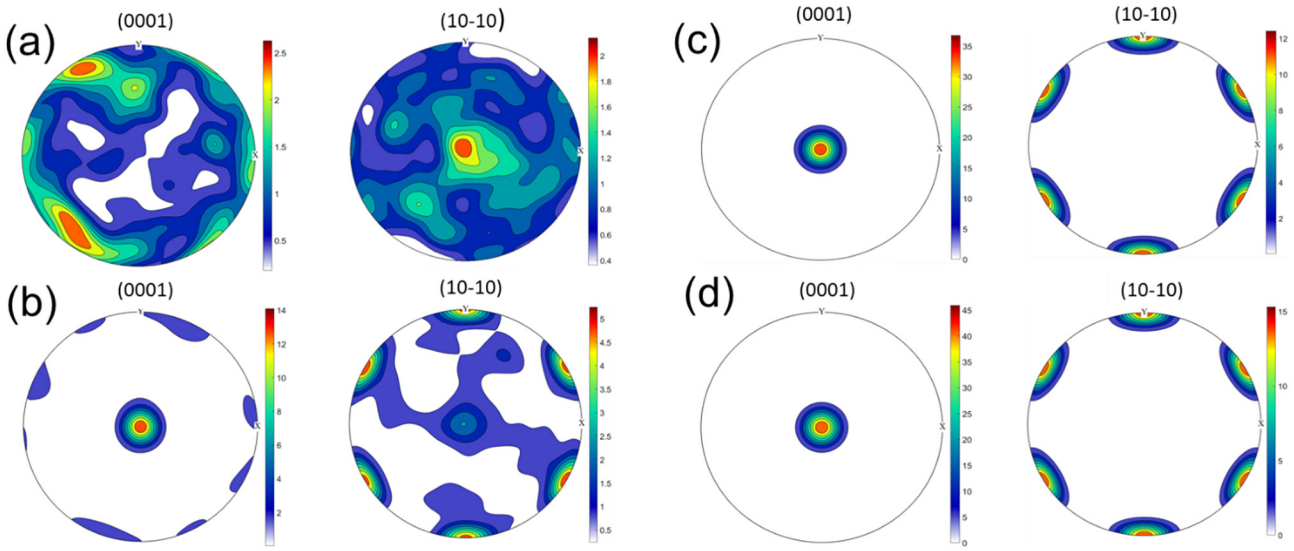

Fig. 7. Pole figures of initial textures: (a) fully random texture; (b) texture intensity 0.5; (c) texture intensity 0.8; (d) single crystal.

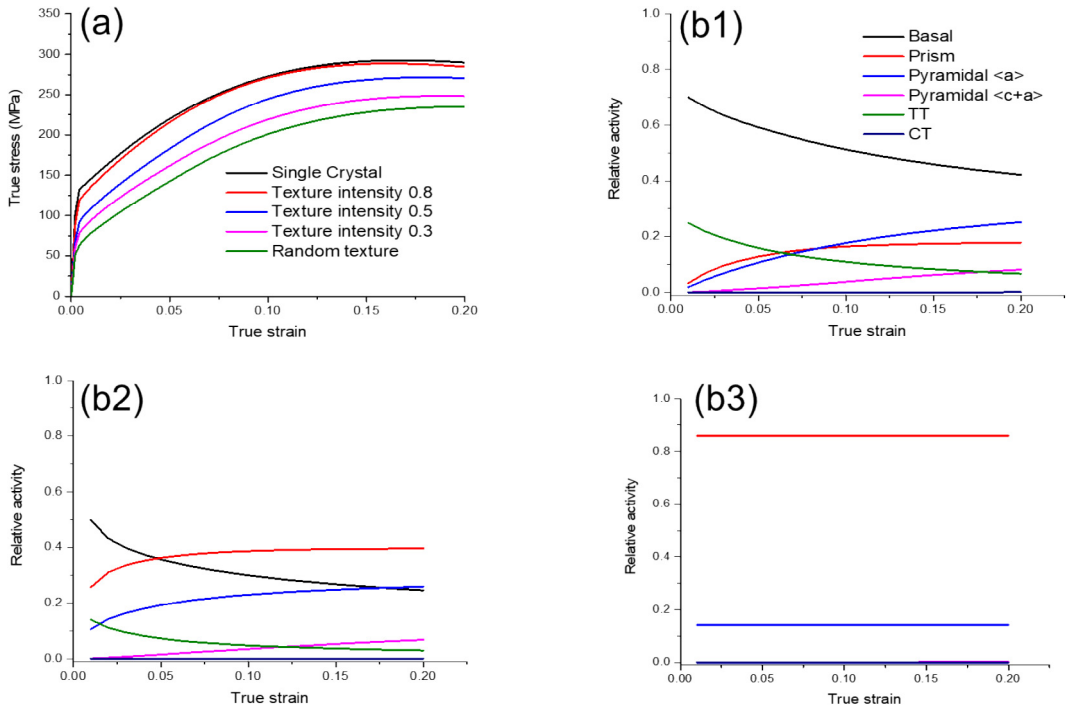

Fig. 8. Effect of texture intensity in TED: (a) true stress-strain curves; (b1) relative activity for random texture; (b2) relative activity for basal texture intensity 0.5; (b3) relative activity for single crystal.

deformation was primarily governed by pyramidal < c + a > slip and partially by CT, which result in the double hardening stress strain curve in Fig. 10(a). However, texture evolution was also influenced by slip as the slip planes tend to reorient parallel to the major deformation axis. This explains as to why the texture after deformation for low initial texture intensities (e.g. texture intensity = 0.5 or fully random texture) were changed marginally when compared with the initial textures in Fig. 7.

4.3. Grain-size effect

The well-known Hall-Petch relationship implies that grain refinement leads to a strengthening of materials [35,36]. The grain-size effect on the mechanical behaviour of AM30 was studied both in TED and CED modes. Five different (average) grain sizes ranging from 10 μm to 200 μm were adopted in the RVE based simulations. For all the grain size based simulations, the microstructures in the RVE model were the same. A representative basal texture intensity of 0.8 was used, with the remaining grains in the RVE assigned a random texture. The dimension of RVE changed with a variation of the grain size (as an example, for grain size $d = 10$ μm, the dimension of RVE was 50 μm, while for grain size $d = 50$ μm, the dimension of RVE was 250 μm). The experimental conditions for tension and compression studies were the same, i.e. T = 293 K and a strain-rate $10^{-1}\,s^{-1}$. This allowed an investigation of the Hall-Petch relationship in both tension and compression deformation modes.

The effect of grain size on the yield stress for these modes are shown in Fig. 13. It is apparent that the yield strength increased with a decrease in the grain size for both tension and compression modes; however, this effect was more evident in the latter case. Dislocation slip dominated the tension deformation along ED. Due to the grain refinement, this dislocation slip was hindered as it encountered an increased number of grain boundaries. In contrast, twinning dominates compression deformation along ED and occurred in the samples with large grains. With an increase in the grain size, more child phases were activated in the material (Fig. 14(b)). Comparing the deformation twins in TED and CED deformation for the samples with the same grain size, fewer twin phases were observed in the tensile deformation (Fig. 14(a)), when compared to the compression deformation model (Fig. 14(b)). The twin volume fractions in TED and CED at ~2% strain of various grain sizes are shown in Fig. 15. The twin volume fraction increases with increasing grain size for both TED and CED, however, the twin volume fraction in CED was much higher than the one in TED for the same grain size. This predicted phenomenon is in good agreement with the experimental result in [37]. However, it should be noted here that it is nearly impossible to make a quantitative comparison of the twinning volume fraction with the data in [37], since fundamentally different materials were studied.

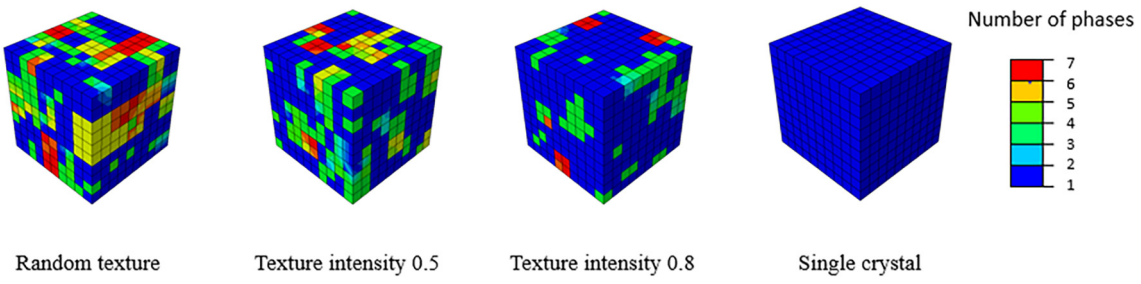

Fig. 9. Effect of texture intensity on the twinning phases in TED.

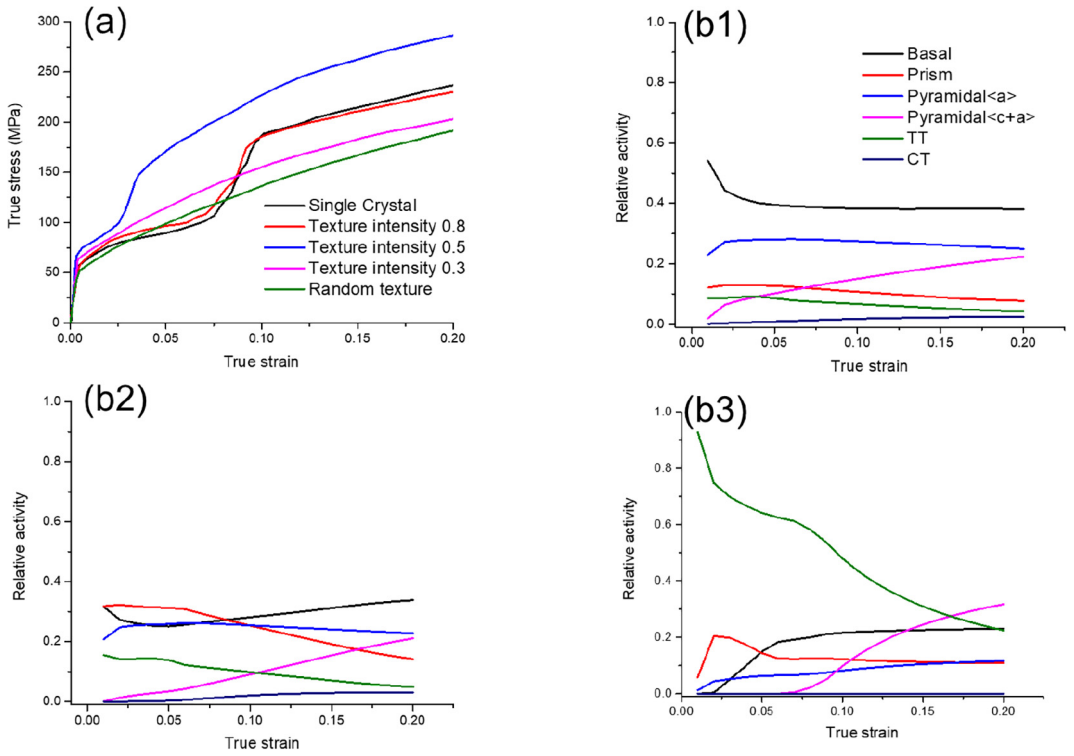

Fig. 10. Effect of texture intensity in CED: (a) true stress-strain curves; (b1) relative activity for random texture; (b2) relative activity for basal intensity 0.5; (b3) relative activity for a single crystal.

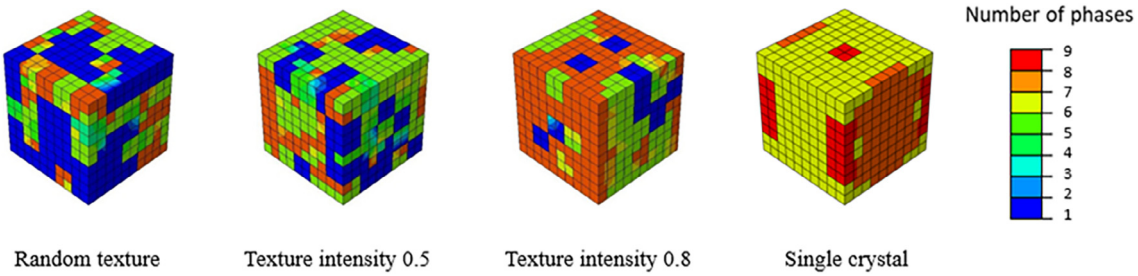

Fig. 11. Effect of texture intensity on twinning phases in CED.

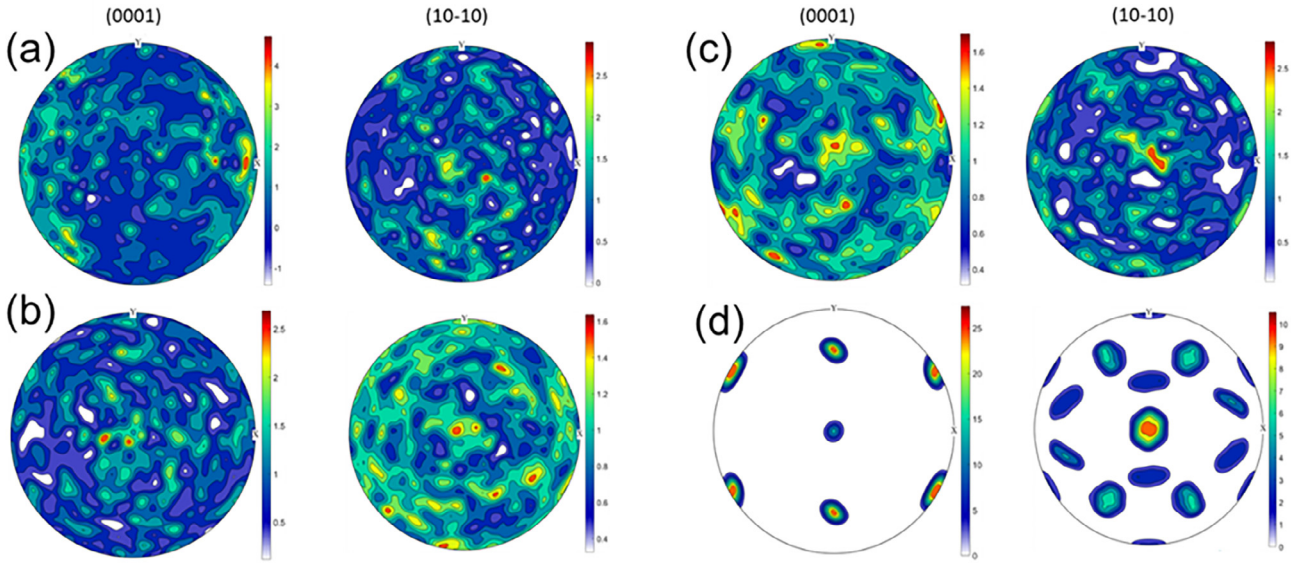

Fig. 12. Pole figures after deformation at 10% strain: (a) fully random texture; (b) texture intensity 0.5; (c) texture intensity 0.8; (d) single crystal.

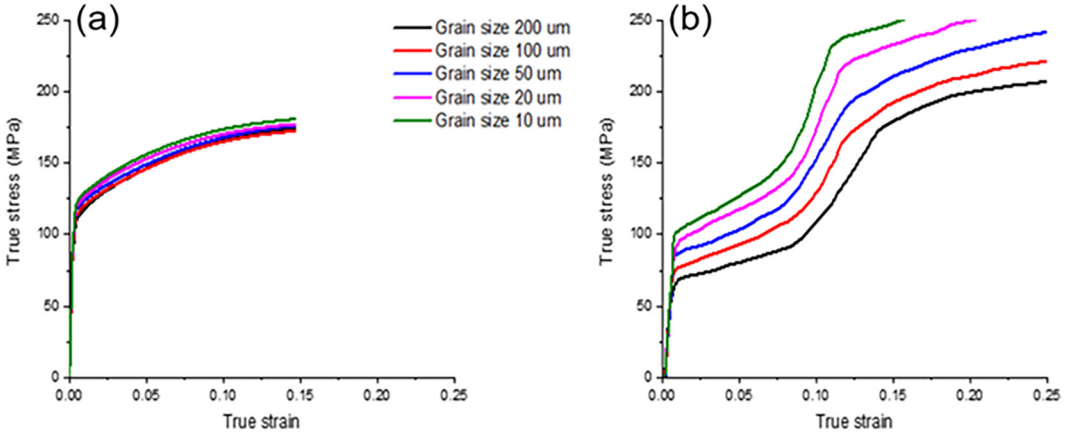

Fig. 13. Effect of grain size on mechanical behaviour of extruded AM30: (a) TED; (b) CED.

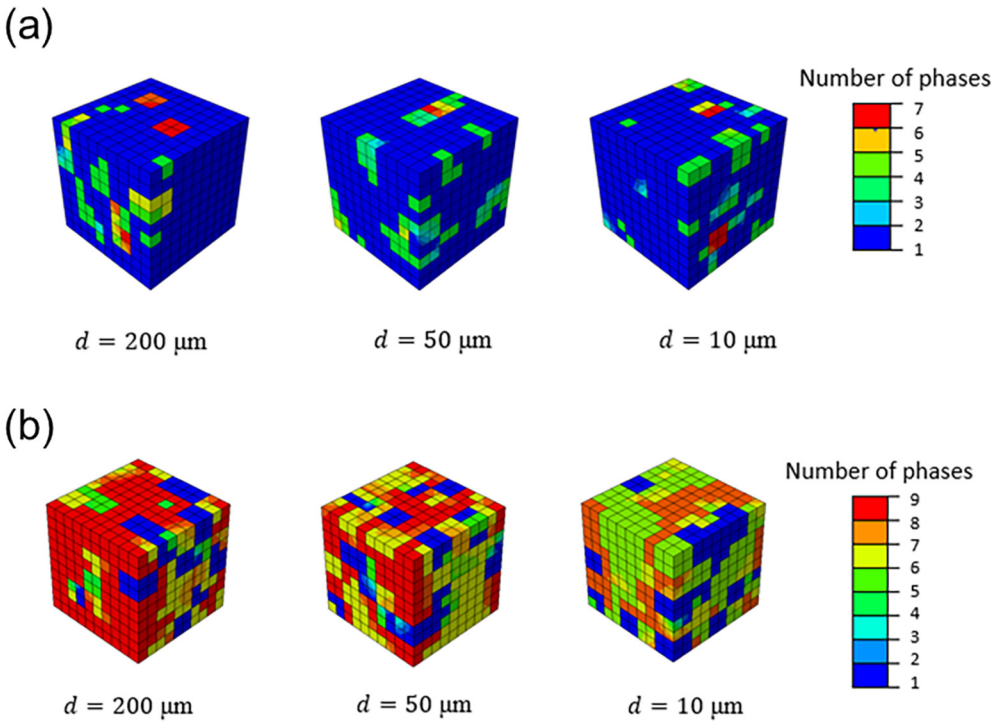

Fig. 14. Number of twin phases for different average grain sizes: (a) TED; (b) CED.

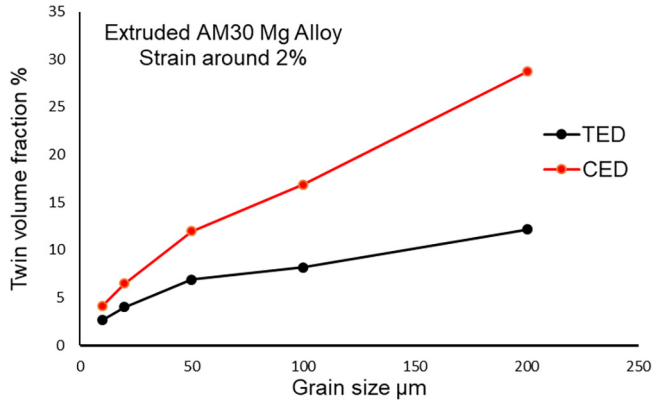

Fig. 15. Variation of twin volume fraction with grain size.

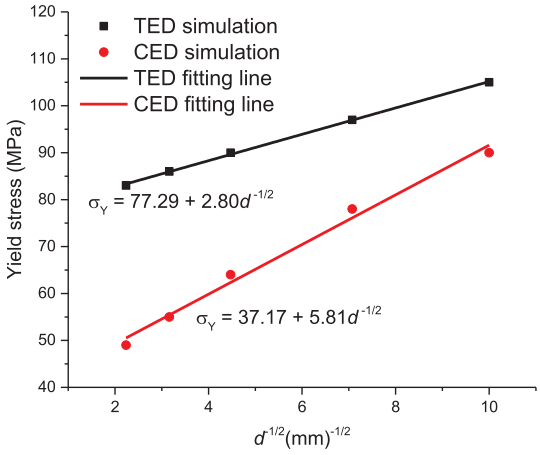

Fig. 16. Grain-size effect on tension-compression yielding asymmetry.

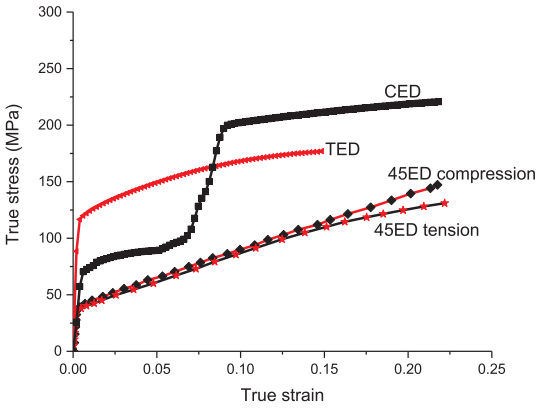

Fig. 17. Effect of loading direction on tension-compression asymmetry.

The presence of twinned phases in a crystal introduced additional boundaries for dislocation motion, resulting in an increase in its resistance to further deformation. This is the reason for the enhanced grain-size effect in compression mode. This also indicates the importance of deformation twinning in the observed yield asymmetry of the studied alloy.

The variations of yield stress with the average grain size for tension and compression tests are shown in Fig. 16. Best-fit curves demonstrated a linear relationship between the yield stress and the inverse square-root of the grain size for both tension and compression. The observed trend of yield stress for both tension and compression increasing with a decrease in grain size was reported in many experimental studies for magnesium alloys (e.g. [8,35,38,39]). The Hall-Petch effect in compression was more pronounced than in tension, which implies that the influence of the grain size on twinning was more than that in dislocation-based slip. Interestingly, an experimentally observed fact of yield asymmetry between compression and tension may be curtailed with grain refinement [5,8,40], was successfully captured by the presented numerical simulations. As shown in Fig. 16, the difference of yield stress between CED and TED was observed to reduce from ~40 MPa at a grain size of 200 μm to ~15 MPa at a grain size of 10 μm.

4.4. Dependence on loading direction

To investigate the effect of loading direction on the tension-compression asymmetry, uniaxial tension and compression at 45° to the extrusion direction (45ED) was studied. Other loading conditions were identical to the samples studied prior (Section 4.1)

A comparison of the true stress-strain responses in uniaxial tension and compression for ED (TED and CED, respectively) and 45ED is shown in Fig. 17. Interestingly, there was an almost negligible tension-compression asymmetry in the 45ED case, although a strong basal texture was present in the material. The relative activity of various deformation modes in tension and compression is shown in Fig. 18. The basal slip dominated the overall deformation, with twinning having a negligible impact. This implies that the twinning-induced deformation was the key factor controlling the tension-compression asymmetry for the magnesium alloy. The texture intensity and grain size indirectly affect this as it was shown to influence twining activity.

5. Concluding remarks

Here, we propose an improved and enhanced crystal-plasticity modelling framework for AM30 especially in context with our prior studies in [20]. This includes:

- improved description for the twin evolution,
- strain-rate and temperature dependent slip and twinning deformation,
- accounting for the effect of grain size and the texture on the mechanical behaviour of the material.

Based on the studies carried out, the following conclusions may be drawn:

1. In the extruded magnesium alloy, there is a strong tension-compression asymmetry, which depends on its initial strong basal texture intensity. A weakening of the basal texture intensity reduces and practically eliminates this asymmetry.
2. The grain size influences the strengthening in this alloy. The Hall-Petch effect was much stronger in compression than in tension. The tension-compression asymmetry was observed to reduce with a decrease in the nominal grain size.
3. The tension-compression asymmetry depended strongly on the loading direction. For loading at 45° to the extrusion direction, this asymmetry vanishes. It is realised that the key factor affecting the observed asymmetry in a certain direction and deformation modes is the deformation twinning.
4. The proposed bottom-up CPFEM model developed in this paper is capable of accounting for the specific features of deformation in magnesium alloys, with no restriction on the grain size, temperature and imposed strain rates.

CRediT authorship contribution statement

Rongxin Zhou: Formal analysis, Investigation, Writing - original draft. **Anish Roy:** Conceptualization, Methodology, Funding acquisition, Supervision, Writing - review & editing. **Vadim V. Silberschmidt:** Writing - review & editing.

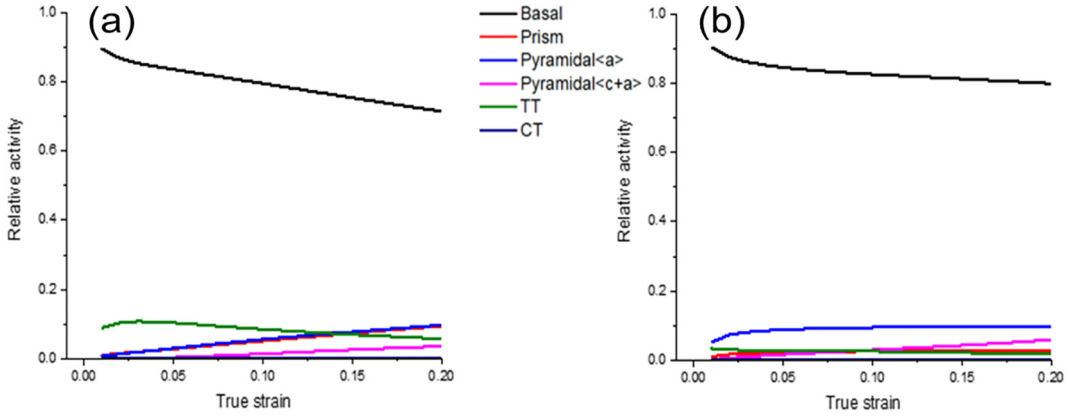

Fig. 18. Relative activity of deformation mode: (a) 45ED tension; (b) 45ED compression.

Acknowledgement

We thank Prof. Satyam Suwas and Dr Anuj Bisht from the Centre for Nanoscience and Engineering, India Institute of Science, Bengaluru, India for the experimental data used in calibrating the CPFEM model. Funding from the EPSRC, United Kingdom (Grant EP/P027555/1), project H^2 Manufacturing is gratefully acknowledged.

Data availability

The raw/processed data required to reproduce these findings cannot be shared at this time as the data also forms part of an ongoing study.

References

[1] S.A. Habib, A.S. Khan, T. Gnäupel-Herold, J.T. Lloyd, S.E. Schoenfeld, Anisotropy, tension-compression asymmetry and texture evolution of a rare-earth-containing magnesium alloy sheet, ZEK100, at different strain rates and temperatures: experiments and modeling, Int. J. Plast. 95 (2017) 163–190, https://doi.org/10.1016/J.IJPLAS.2017.04.006.

[2] N. Chandola, R.A. Lebensohn, O. Cazacu, B. Revil-Baudard, R.K. Mishra, F. Barlat, Combined effects of anisotropy and tension–compression asymmetry on the torsional response of AZ31 Mg, Int. J. Solids Struct. 58 (2015) 190–200, https://doi.org/10.1016/J.IJSOLSTR.2015.01.001.

[3] N.V. Dudamell, I. Ulacia, F. Gálvez, S. Yi, J. Bohlen, D. Letzig, I. Hurtado, M.T. Pérez-Prado, Twinning and grain subdivision during dynamic deformation of a Mg AZ31 sheet alloy at room temperature, Acta Mater. 59 (2011) 6949–6962, https://doi.org/10.1016/J.ACTAMAT.2011.07.047.

[4] M. Kavyani, G.R. Ebrahimi, M. Sanjari, M. Haghshenas, Texture evaluation in warm deformation of an extruded Mg–6Al–3Zn alloy, J. Magnes. Alloy. 4 (2016) 89–98, https://doi.org/10.1016/J.JMA.2016.05.002.

[5] L. Wang, E. Mostaed, X. Cao, G. Huang, A. Fabrizi, F. Bonollo, C. Chi, M. Vedani, Effects of texture and grain size on mechanical properties of AZ80 magnesium alloys at lower temperatures, Mater. Des. 89 (2016) 1–8, https://doi.org/10.1016/J.MATDES.2015.09.153.

[6] F. Li, X. Zeng, Q. Chen, G.J. Cao, Effect of local strains on the texture and mechanical properties of AZ31 magnesium alloy produced by continuous variable cross-section direct extrusion (CVCDE), Mater. Des. 85 (2015) 389–395, https://doi.org/10.1016/J.MATDES.2015.06.168.

[7] E. Mostaed, A. Fabrizi, D. Dellasega, F. Bonollo, M. Vedani, Microstructure, mechanical behavior and low temperature superplasticity of ECAP processed ZM21 Mg alloy, J. Alloys Compd. 638 (2015) 267–276, https://doi.org/10.1016/J.JALLCOM.2015.03.029.

[8] S.M. Yin, C.H. Wang, Y.D. Diao, S.D. Wu, S.X. Li, Influence of grain size and texture on the yield asymmetry of Mg-3Al-1Zn alloy, J. Mater. Sci. Technol. 27 (2011) 29–34, https://doi.org/10.1016/S1005-0302(11)60021-2.

[9] L.B. Tong, M.Y. Zheng, S. Kamado, D.P. Zhang, J. Meng, L.R. Cheng, H.J. Zhang, Reducing the tension–compression yield asymmetry of extruded Mg–Zn–Ca alloy via equal channel angular pressing, J. Magnes. Alloy. 3 (2015) 302–308, https://doi.org/10.1016/J.JMA.2015.08.007.

[10] L. Zhang, W. Zhang, B. Cao, W. Chen, J. Duan, G. Cui, Effects of texture and grain size on the yield strength of ZK61 alloy rods processed by cyclic extrusion and compression, Mater. (Basel, Switzerland) 10 (2017), https://doi.org/10.3390/ma10111234.

[11] S. Kamrani, C. Fleck, Effects of calcium and rare-earth elements on the microstructure and tension–compression yield asymmetry of ZEK100 alloy, Mater. Sci. Eng. A 618 (2014) 238–243, https://doi.org/10.1016/J.MSEA.2014.09.023.

[12] J. Jain, W.J. Poole, C.W. Sinclair, M.A. Gharghouri, Reducing the tension–compression yield asymmetry in a Mg–8Al–0.5Zn alloy via precipitation, Scr. Mater. 62 (2010) 301–304, https://doi.org/10.1016/J.SCRIPTAMAT.2009.11.024.

[13] C. Ma, A. Chapuis, X.Q. Guo, L.Y. Zhao, P.D. Wu, Q. Liu, X.B. Mao, Modeling the deformation behavior of a rolled Mg alloy with the EVPSC-TDT model, Mater. Sci. Eng. A (2017), https://doi.org/10.1016/j.msea.2016.11.027.

[14] I. Chelladurai, D. Adams, D.T. Fullwood, M.P. Miles, S. Niezgoda, I.J. Beyerlein, M. Knezevic, Modeling of trans-grain twin transmission in AZ31 via a neighborhood-based viscoplastic self-consistent model, Int. J. Plast. (2018), https://doi.org/10.1016/J.IJPLAS.2018.03.012.

[15] Y. Gan, W. Song, J. Ning, H. Tang, X. Mao, An elastic–viscoplastic crystal plasticity modeling and strain hardening for plane strain deformation of pure magnesium, Mech. Mater. 92 (2016) 185–197, https://doi.org/10.1016/J.MECHMAT.2015.09.012.

[16] B. Liu, D. Raabe, F. Roters, P. Eisenlohr, R.A. Lebensohn, Modelling and simulation in materials science and engineering comparison of finite element and fast Fourier transform crystal plasticity solvers for texture prediction, IOP Publ. Model. Simul. Mater. Sci. Eng. Model. Simul. Mater. Sci. Eng. 18 (2010) 21, https://doi.org/10.1088/0965-0393/18/8/085005.

[17] F. Kabirian, A.S. Khan, T. Gnäupel-Herlod, Visco-plastic modeling of mechanical responses and texture evolution in extruded AZ31 magnesium alloy for various loading conditions, Int. J. Plast. (2015), https://doi.org/10.1016/j.ijplas.2014.10.012.

[18] M. Ardeljan, I.J. Beyerlein, B.A. McWilliams, M. Knezevic, Strain rate and temperature sensitive multi-level crystal plasticity model for large plastic deformation behavior: application to AZ31 magnesium alloy, Int. J. Plast. (2016), https://doi.org/10.1016/j.ijplas.2016.04.005.

[19] J. Zhang, S.P. Joshi, Phenomenological crystal plasticity modeling and detailed micromechanical investigations of pure magnesium, J. Mech. Phys. Solids (2012), https://doi.org/10.1016/j.jmps.2012.01.005.

[20] Q. Liu, A. Roy, V.V. Silberschmidt, Temperature-dependent crystal-plasticity model for magnesium: a bottom-up approach, Mech. Mater. (2017), https://doi.org/10.1016/j.mechmat.2017.07.008.

[21] H. Wang, P.D. Wu, J. Wang, C.N. Tomé, A crystal plasticity model for hexagonal close packed (HCP) crystals including twinning and de-twinning mechanisms, Int. J. Plast. (2013), https://doi.org/10.1016/j.ijplas.2013.02.016.

[22] J. Cheng, S. Ghosh, A crystal plasticity FE model for deformation with twin nucleation in magnesium alloys, Int. J. Plast. (2015), https://doi.org/10.1016/j.ijplas.2014.10.005.

[23] J. Cheng, S. Ghosh, Crystal plasticity finite element modeling of discrete twin evolution in polycrystalline magnesium, J. Mech. Phys. Solids. 99 (2017) 512–538, https://doi.org/10.1016/J.JMPS.2016.12.008.

[24] J.W. Hutchinson, Bounds and self-consistent estimates for creep of polycrystalline materials, Proc. R. Soc. A Math. Phys. Eng. Sci. 348 (1976) 101–127, https://doi.org/10.1098/rspa.1976.0027.

[25] L. Jiang, J.J. Jonas, R.K. Mishra, A.A. Luo, A.K. Sachdev, S. Godet, Twinning and texture development in two Mg alloys subjected to loading along three different strain paths, Acta Mater. 55 (2007) 3899–3910, https://doi.org/10.1016/J.ACTAMAT.2007.03.006.

[26] A. Ghaderi, M.R. Barnett, Sensitivity of deformation twinning to grain size in titanium and magnesium, Acta Mater. 59 (2011) 7824–7839, https://doi.org/10.1016/J.ACTAMAT.2011.09.018.

[27] V. Kannan, K. Hazeli, K.T. Ramesh, The mechanics of dynamic twinning in single crystal magnesium, J. Mech. Phys. Solids 120 (2018) 154–178, https://doi.org/10.1016/J.JMPS.2018.03.010.

[28] R.J. Asaro, Crystal plasticity, J. Appl. Mech. 50 (1983) 921, https://doi.org/10.1115/1.3167205.

[29] L. Capolungo, I.J. Beyerlein, G.C. Kaschner, C.N. Tomé, On the interaction between slip dislocations and twins in HCP Zr, Mater. Sci. Eng. A 513–514 (2009) 42–51, https://doi.org/10.1016/J.MSEA.2009.01.035.

[30] L. Capolungo, I.J. Beyerlein, C.N. Tomé, Slip-assisted twin growth in hexagonal close-packed metals, Scr. Mater. 60 (2009) 32–35, https://doi.org/10.1016/J.SCRIPTAMAT.2008.08.044.

[31] A. Acharya, A. Roy, Size effects and idealized dislocation microstructure at small scales: predictions of a phenomenological model of mesoscopic field dislocation mechanics: Part I, J. Mech. Phys. Solids 54 (2006) 1687–1710, https://doi.org/10.1016/J.JMPS.2006.01.009.

[32] A. Acharya, Jump condition for GND evolution as a constraint on slip transmission at grain boundaries, Philos. Mag. Taylor & Francis Group, 2007, pp. 1349–1359, , https://doi.org/10.1080/14786430600951537.

[33] Y. Huang, A User-material subroutine incorporating single crystal plasticity in the ABAQUS finite element program. Mech report 178, Division of Engineering and Applied Sciences, Harvard University, 1991. http://www.columbia.edu/~jk2079/fem/umat_documentation.pdf (accessed March 27, 2019).

[34] Y. Wang, H. Choo, Influence of texture on Hall-Petch relationships in an Mg alloy, Acta Mater. 81 (2014) 83–97, https://doi.org/10.1016/J.ACTAMAT.2014.08.023.

[35] H. Yu, Y. Xin, M. Wang, Q. Liu, Hall-Petch relationship in Mg alloys: a review, J. Mater. Sci. Technol. 34 (2018) 248–256, https://doi.org/10.1016/j.jmst.2017.07.022.

[36] J. Peng, Z. Zhang, Z. Liu, Y. Li, P. Guo, W. Zhou, Y. Wu, The effect of texture and grain size on improving the mechanical properties of Mg-Al-Zn alloys by friction stir processing, Sci. Rep. 8 (2018) 4196, https://doi.org/10.1038/s41598-018-22344-3.

[37] D.L. Yin, J.T. Wang, J.Q. Liu, X. Zhao, On tension–compression yield asymmetry in an extruded Mg–3Al–1Zn alloy, J. Alloys Compd. 478 (2009) 789–795, https://doi.org/10.1016/J.JALLCOM.2008.12.033.

[38] J. Lin, W. Ren, Q. Wang, L. Ma, Y. Chen, Influence of grain size and texture on the yield strength of mg alloys processed by severe plastic deformation, Adv. Mater. Sci. Eng. 2014 (2014) 1–9, https://doi.org/10.1155/2014/356572.

[39] L. Guo, Z. Chen, L. Gao, Effects of grain size, texture and twinning on mechanical properties and work-hardening behavior of AZ31 magnesium alloys, Mater. Sci. Eng. A 528 (2011) 8537–8545, https://doi.org/10.1016/J.MSEA.2011.07.076.

[40] W. Yuan, R.S. Mishra, Grain size and texture effects on deformation behavior of AZ31 magnesium alloy, Mater. Sci. Eng. A 558 (2012) 716–724, https://doi.org/10.1016/J.MSEA.2012.08.080.